RSC Advances

PAPER

View Article Online
View Journal | View Issue

Cite this: *RSC Adv.*, 2015, **5**, 99037

Solid-state graphene formation *via* a nickel carbide intermediate phase†

W. Xiong,‡[a] Y. S. Zhou,‡[a] W. J. Hou,[a] T. Guillemet,[ab] J. F. Silvain,[ab] Y. Gao,[a] M. Lahaye,[b] E. Lebraud,[b] S. Xu,[c] X. W. Wang,[c] D. A. Cullen,[d] K. L. More,[d] L. Jiang[e] and Y. F. Lu*[a]

Received 12th September 2015
Accepted 4th November 2015

DOI: 10.1039/c5ra18682j

www.rsc.org/advances

Direct formation of graphene with a controlled number of graphitic layers on dielectric surfaces is highly desired for practical applications but still challenging. Distinguished from the conventional chemical vapor deposition methods, a solid-state rapid thermal processing (RTP) method can achieve high-quality graphene formation on dielectric surfaces without transfer. However, little research is available to elucidate the graphene growth mechanism in the RTP method (heating rate ~15 °C s^{-1}). Here we show a solid-state transformation mechanism in which a metastable nickel carbide (Ni_3C) intermediate phase plays a critical role in transforming amorphous carbon to two dimensional crystalline graphene and contributing to the autonomous Ni evaporation in the RTP process. The formation, migration and decomposition of Ni_3C are confirmed to be responsible for graphene formation and Ni evaporation. The Ni_3C-assisted graphene formation mechanism expands the understanding of Ni-catalyzed graphene formation and provides insightful guidance for controlled growth of graphene through the solid-state transformation process.

Introduction

Electronic-grade graphene has been regarded as one of the most promising building blocks for future electronics and optoelectronics.[1–3] Since the first graphene flake was isolated *via* a Scotch® tape method in 2004,[4] the unique two dimensional (2D) lattice structure and outstanding properties of graphene have triggered a wave in both fundamental research and practical applications, covering a broad range of fields. Thus far, scalable growth of electronic-grade graphene can be obtained *via* chemical vapor deposition (CVD) of hydrocarbons and thermal decomposition of silicon carbide (SiC) wafers.

Several graphene growth mechanisms have been studied. In CVD methods, depending on the carbon solubility in the metals, two growth mechanisms, (1) surface catalytic growth and (2) carbon dissolving and precipitation, have been reported to explain the CVD growth of graphene on copper (Cu) and carbon-soluble transition metals (such as nickel (Ni), cobalt (Co), ruthenium (Ru) and iridium (Ir)), respectively.[5] Similar carbon dissolving and precipitation mechanisms have also been applied in explaining the Ni-catalyzed transformation of solid carbon sources, such as polymers and amorphous carbon, into graphene.[6–9] On the other hand, in the thermal decomposition of SiC, graphene formation is ascribed to the thermal evaporation of silicon (Si) atoms and the reconstruction of carbon (C) atoms on SiC surfaces to form a honeycomb graphene crystalline structure.[10] It is noteworthy that most of the mechanism studies are based on slow heating processes (heating rate < 5 °C s^{-1}). Graphene growth *via* rapid thermal processing (RTP, heating rate ~15 °C s^{-1}) has not been systematically investigated and well understood.

For practical applications, deposition of graphene with a controlled number of layers on dielectric surfaces is required. Present methods, however, usually involve multi-step processing and graphene transfers which can easily degrade the quality of graphene by introducing extra defects, wrinkles and contaminants and are unfavorable for large-scale production. Therefore, single-step direct deposition of graphene on dielectric surfaces with a controllable number of layers is strongly desired. Recently, RTP of solid Ni–C thin films was used to directly deposit graphene on dielectric surfaces at wafer scale accompanied by autonomous Ni evaporation,[11] thus eliminating the need for post-growth transferring processes. By tuning Ni–C ratios, the number of graphene layers was precisely controlled in the single-step RTP process. However, the RTP graphene growth and Ni evaporation cannot be satisfactorily

[a]*Department of Electrical Engineering, University of Nebraska-Lincoln, Lincoln, NE 68588, USA. E-mail: ylu2@unl.edu*

[b]*Institut de Chimie de la Matière Condensée de Bordeaux, Avenue du Docteur Albert Schweitzer, F-33608, Pessac Cedex, France*

[c]*Department of Mechanical Engineering, Iowa State University, Ames, IA 50011, USA*

[d]*Materials Science & Technology Division, Oak Ridge National Laboratory, Oak Ridge, TN 37831, USA*

[e]*Laser Micro/Nano Fabrication Laboratory, School of Mechanical Engineering, Beijing Institute of Technology, Beijing 100081, China*

† Electronic supplementary information (ESI) available. See DOI: 10.1039/c5ra18682j

‡ Those authors contributed equally.

explained by the existing mechanisms. Therefore, an in-depth understanding of the graphene growth mechanism during the RTP process is needed to realize precise control of graphene growth and achieve the full potential of RTP for graphene production.

In this study, a solid-state transformation mechanism in the RTP process was revealed by investigating the temperature-resolved evolution of Ni–C thin films using Auger electron spectroscopy (AES) depth profiling and glancing-angle X-ray diffraction (GAXRD). It was discovered that the formation and decomposition of a metastable hexagonal nickel carbide (Ni_3C) phase plays a critical role in graphene formation and Ni evaporation during the solid-state RTP processes.

Experimental section

Growth of graphene

Dielectric wafers were first cleaned by a standard cleaning process.[12] The cleaned wafers were coated with an amorphous C film of 5 nm and a Ni film of 65 nm sequentially by direct current (DC) magnetron sputtering using graphite (Kurt J. Lesker, 99.999% purity) and nickel (Kurt J. Lesker, 99.995% purity) targets at room temperature. The Ni/C-coated wafers were then loaded into an RTP system (MTI, OTF-1200X-4-RTP). The RTP tube was repeatedly purged with high-purity argon (Ar) gas for 3–5 times to remove air from the tube. Then the RTP tube was pumped down and maintained at 20 mTorr. The RTP process started at room temperature, heated up to 1100 °C at a rate of 15 °C s^{-1}, kept at 1100 °C for 2 min and cooled down to room temperature at a rate of 1 °C s^{-1}. The wafers were taken out for characterization without further post-growth treatments.

Raman characterization

The Raman characterization of the graphene samples was conducted using a Renishaw InVia Raman microscope with an excitation wavelength of 514.5 nm and a lateral resolution of ~1 μm. The Raman mapping was carried out with a grip spacing of 0.25 μm and an accumulation time of 3 s at each spot.

Transmission electron microscopy characterization

TEM images were acquired using a Hitachi HF-3300 FE-TEM, and scanning transmission electron microscopy (STEM) images were recorded using a Nion UltraSTEM 100 operated at 60 kV. Specimens for STEM analysis were prepared by graphene transfer from silicon dioxide/silicon (SiO_2/Si) substrates to Cu grids through poly(methyl methacrylate) (PMMA) coating and subsequent SiO_2 layer etching processes.

Auger electron spectroscopy analysis

The AES analysis was conducted with a Thermo Microlab 310F Auger electron spectrometer. The same Ni/C thin film samples annealed at different temperatures, including room temperature (RT), 200, 400, 800, 1000 and 1100 °C which were used for the characterization. Ar^+ ions were used in the depth profiling for etching the Ni/C thin films. The ionic etching parameters were as follows: etching speed, 0.2 nm s^{-1}; acceleration voltage, 3.5 kV; current intensity, 0.35 μA; and scanning area, 1 × 1 mm^2. The parameters for AES analysis were as follows: acceleration voltage, 10 kV; current intensity, 10 nA; and scanning area, 5 × 5 μm^2. Ni_{LMM}, O_{KLL}, Si_{LVV}, and C_{KVV} Auger lines were used for plotting the depth profiles of each sample.

Glancing-angle X-ray diffraction

The GAXRD characterization of the Ni/C thin films were conducted using a high-resolution X-ray diffractometer with a copper anticathode (Bruker, D8 Discover). The X-ray tube inclination relative to the Ni/C sample was 1°. The working intensity and voltage used in the GAXRD characterization were 40 mA and 40 kV, respectively.

Results and discussion

Fig. 1 illustrates the schematic of the solid-state transformation process for graphene growth. The whole process consists of sputter depositing amorphous C (a-C) and Ni thin films sequentially onto a dielectric substrate (Fig. 1a), followed by an RTP process at 1100 °C for a couple of minutes (typically 2 min). It was found that in the low-temperature annealing stage (RT ~400 °C), the a-C diffuses into the Ni top layer and forms a metastable hexagonal close-packed (hcp) Ni_3C structure, as shown in Fig. 1b. As the temperature increases, the as-formed Ni_3C film starts to decompose and leads to carbon-induced Ni evaporation due to its weak Ni–C bonds.[13,14] During the high-temperature annealing stage (800–1100 °C), the metastable Ni_3C transforms gradually into graphene accompanied by the autonomous evaporation of Ni (Fig. 1c). By the end of the Ni evaporation, uniform graphene is deposited on the dielectric surfaces (Fig. 1d). The requirement for post-growth Ni etching and graphene transfer is eliminated. Further, there is no need of gaseous hydrocarbon precursors in the process which significantly simplifies the facility support. Fig. 2 shows the results of the controlled RTP growth of graphene. The quality and uniformity of the RTP graphene was characterized using Raman spectroscopy by mapping I_{2D}/I_G ratio as shown in Fig. 2a–c. It is generally accepted that an I_{2D}/I_G ratio located between 0.8 and 1.4 represents the formation of bi-layer graphene.[15,16] Thus, by mapping I_{2D}/I_G ratio, graphene sheets of different layer numbers can be well discerned. Regions of different colors represent the graphene of different number of layers. The uniform color distribution in Fig. 2a–c indicates that graphene sheets with controlled graphene sheets have been obtained by the RTP method. The coverages of the graphene sheets with mono-layer, bi-layer, and tri-layer graphene are 92.2%, 95.1%, 67.5%, respectively. TEM characterization of the graphene sheets in cross-sectional and top views (as shown in Fig. 2d–f and S1,† respectively) further confirm the controlled growth of graphene sheets with one, two and three atomic layers.

To establish an in-depth understanding of the Ni evaporation in the RTP process, a control experiment was conducted using two different samples with and without the a-C sandwich

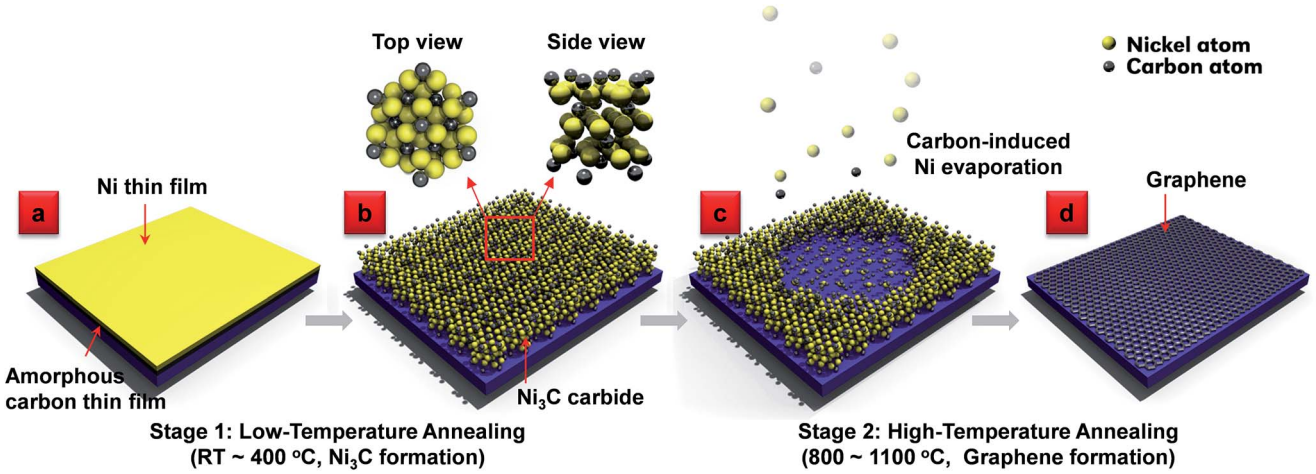

Fig. 1 Schematic illustration of the solid-state transformation procedure for graphene growth in the RTP process, including (a) Ni/C deposition, (b)Ni_3C formation, (c) Ni_3C decomposition and Ni evaporation, and (d) graphene formation.

layer. Two fused silica wafers coated with Ni/a-C and Ni thin films, respectively, (denoted as A and B in Fig. 2g) were subjected to the same RTP process at 1100 °C for 2 min. The Ni-coated silica substrate (Sample B) did not show any obvious change after the RTP process. However, the Ni top layer evaporated from the Ni/a-C coated silica wafer (Sample A) after the

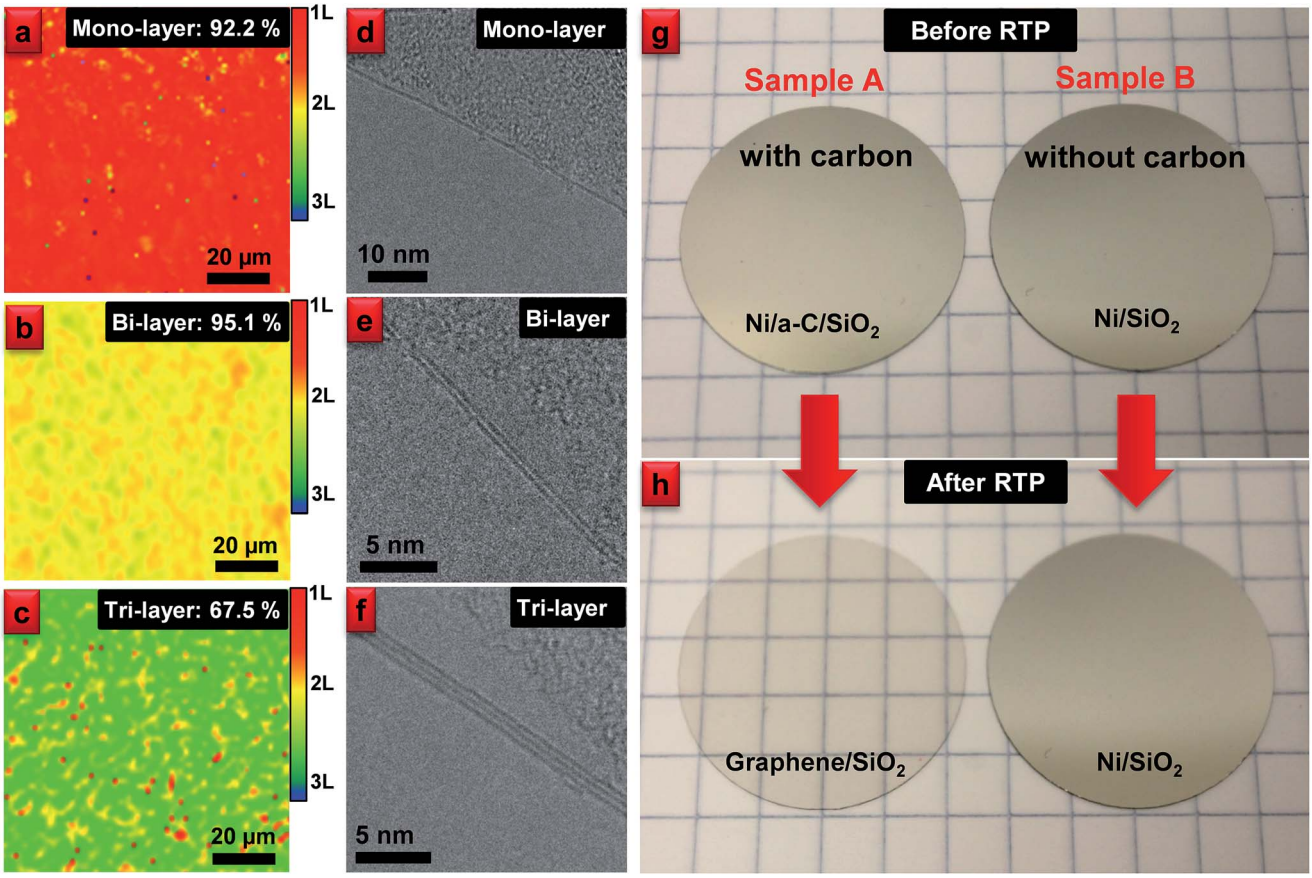

Fig. 2 Controlled graphene growth *via* the RTP process. (a–c) Large area Raman mapping images of the as-grown mono-layer, bi-layer and tri-layer graphene, respectively. (d–f) Transmission electron microscopy images of the as-grown mono-layer, bi-layer and tri-layer graphene. (g) A photo showing two fused silica wafers coated with "Sample A": Ni (65 nm)/a-C (5 nm) thin film and "Sample B": Ni (65 nm) thin film, respectively, before the RTP process. (h) A photo showing the fused silica wafers after the RTP process. The wafer "A" becomes highly transparent after the RTP process, indicating the effective Ni evaporation during the RTP process. In contrast, no Ni evaporation occurs on wafer "B" after the RTP process.

RTP process, which is clearly evidenced by the change in the surface appearance (Fig. 2h) of Sample A and weight loss experiments (ESI: Table S2†). Considering the high boiling temperature of Ni (2913 °C), the RTP processing temperature of 1100 °C is too low to evaporate Ni. Therefore, the existence of the sandwiched carbon layer is critical for the evaporation of Ni.

We conducted a temperature-resolved AES depth profiling analysis of the annealed Ni/C/SiO_2 samples. AES is a surface sensitive technique and can be used to analyze the chemical components of the annealed samples.[17,18] Six batches of Ni/C/SiO_2 samples were prepared with the same Ni/C film structure (Ni: 60 nm, C: 10 nm) and subjected to RTP treatments at different annealing temperatures, including room temperature (no annealing), 200, 400, 600, 1000 and 1100 °C. Fig. 3 shows the temperature-resolved AES depth profiling results. For the sample without annealing (room temperature), a layer of non-carbidic C, which is denoted as the sputtered a-C layer, was observed to be sandwiched between the Ni layer and the SiO_2 substrate. A very thin layer of carbidic C was also observed between a-C and Ni, indicating the formation of a small amount of Ni_3C as a result of the sputtering process (Fig. 3a), which coincides with published results.[19] As the annealing temperature increased to 200 °C, the concentration of carbidic C significantly increased at the Ni/a-C interface accompanied by a decreased a-C concentration under the Ni_3C layer (Fig. 3b), indicating the diffusion of a-C into the Ni layer and the formation of Ni_3C at the elevated temperature. As the annealing temperature further increased to 400 °C, the carbidic C became the major carbon phase observed at the Ni/SiO_2 interface (Fig. 3c and S1d†), indicating the complete diffusion of carbon atoms into the Ni layer and formation of a layer of Ni_3C at the Ni/SiO_2 interface. As the RTP annealing temperature increased to 800 °C, the carbide signal decreased at the Ni/SiO_2 interface, accompanied by an increase of graphitic C at the Ni surface region (Fig. 3d). The AES results suggest that the Ni_3C starts to decompose at an elevated temperature above 400 °C and converts the carbidic C to the graphitic C. The AES depth profiling also shows that there is a significant amount of bulk-to-surface diffusion of carbon atoms within the Ni at temperatures above 400 °C (Fig. 3d). When annealed at 1000 °C, more graphitic C diffuses to the top of the Ni surface (Fig. 3e). Meanwhile, the overall thickness of the Ni layer is reduced from 60 nm to 40 nm, indicating the gradual loss of nickel. Finally, after it was annealed at 1100 °C for 2 min, the Ni top layer evaporated leaving graphitic C (graphene) on top of the SiO_2 surface (Fig. 3f). According to the AES results, obvious Ni loss starts at a temperature of 800 °C and above evidenced by the reduced Ni thickness at the high-temperature annealing stage, accompanied by the continuous depletion of Ni_3C and the formation of graphene. It should be noted that the AES signals of graphitic C and carbidic C looks quite similar to each other with only a small difference in AES lineshape. Therefore, we cannot well discern the carbidic C and graphitic carbon by using the AES depth profiling only. The carbon profile as shown in Fig. 3d and e may contain both graphitic and carbidic C signals.

To further characterize the annealed Ni/C samples, temperature-resolved evolution of Ni/C samples was also investigated by GAXRD (Fig. 4). Three peaks in the XRD spectra (Peaks A, B, C) were studied, as shown in Fig. 4a. Peak A was

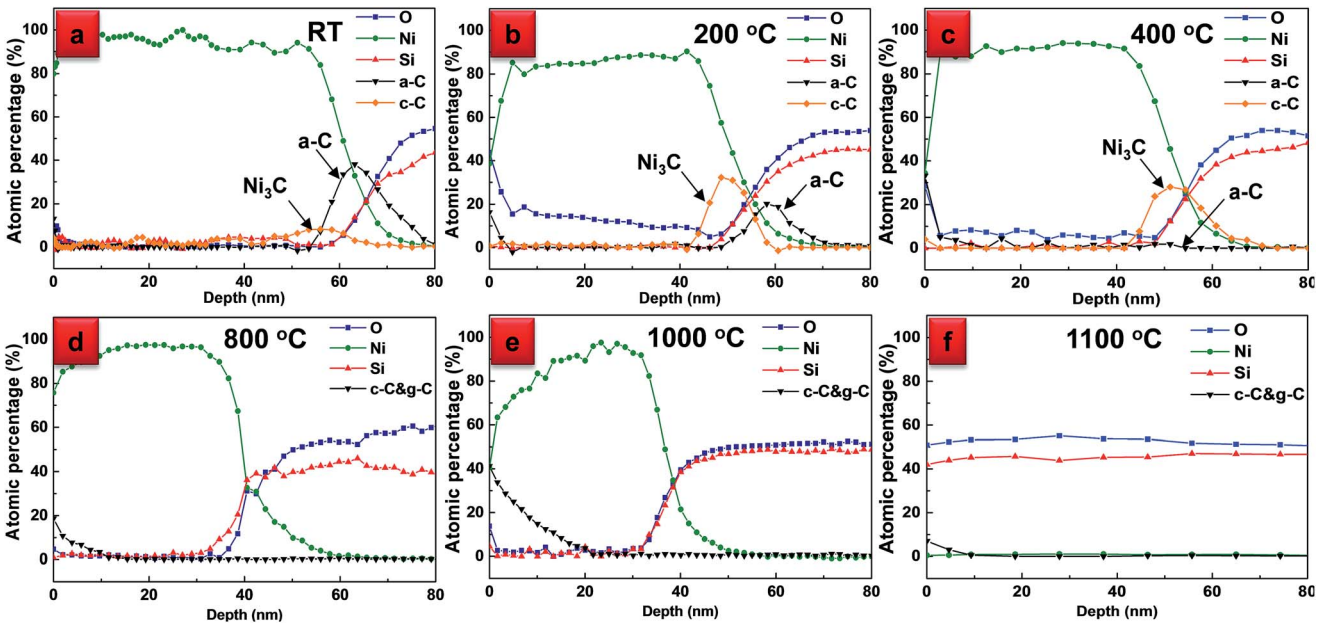

Fig. 3 Temperature-resolved Auger electron spectroscopy (AES) depth profiling analysis of Ni/C sample. (a–f) show the AES depth profiling diagrams after 2 min annealing at room temperature (RT), 200, 400, 800, 1000 and 1100 °C, respectively. Auger lines of Ni_{LMM}, O_{KLL}, Si_{LVV} and C_{KVV} are plotted in an atomic percentage diagram as a function of the milling depth from the sample surface towards the SiO_2 interface. The Ni, amorphous C (a-C), carbidic C (c-C), O and Si signals are denoted in green, black, orange, blue and red, respectively. In (d–f) the "c-C&g-C" represents the total percentage of carbidic C and graphitic C.

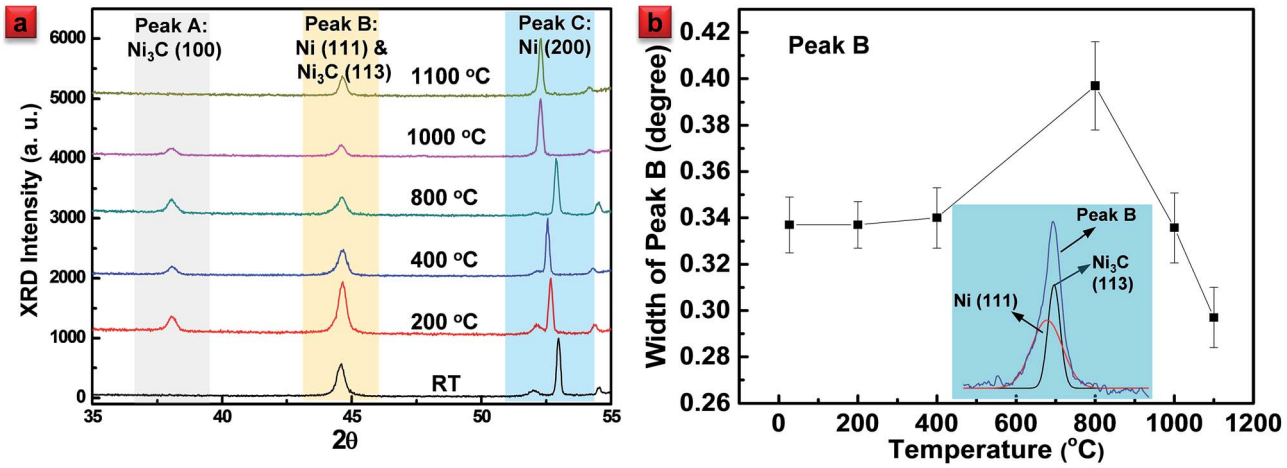

Fig. 4 Temperature-resolved glancing-angle XRD (GAXRD) analysis of Ni/C samples annealed at different temperatures (*i.e.*, RT, 200, 400, 800, 1000, 1100 °C). (a) GAXRD spectra of the Ni/C samples with the highlights of the peaks A, B and C. (b) The GAXRD peak width (Peak B) of the Ni/C samples as a function of annealing temperature. The inset shows Ni(111) and Ni_3C (113) components of Peak B.

ascribed to the Ni_3C(100) peak, which was observed in all samples except for those without RTP treatment (denoted as "RT" sample), and the sample was annealed at 1100 °C (denoted as "1100 °C-annealed" sample in the following text). The absence of the Ni_3C(100) peak in the RT sample and the 1100 °C-annealed sample was ascribed to insufficient Ni_3C formation at room temperature and the complete decomposition of Ni_3C at 1100 °C, respectively, which coincides with the AES results. Peak B in Fig. 4a consisted of two components, the Ni(111) peak at 44.51° and the Ni_3C(113) peak at 44.85°, which were too close to be distinguished as two individual peaks. To facilitate the analysis, the full width at half maximum (FWHM) of Peak B as a function of the RTP annealing temperature was plotted in Fig. 4b. Since the presence of Ni_3C broadened Peak B, the FWHM of Peak B qualitatively reflected the existence and the amount of Ni_3C in the Ni/C thin films. Fig. 4b shows that the FWHM of Peak B increased as the annealing temperature increased from RT to 800 °C, indicating the increased concentration of Ni_3C with respect to Ni as the annealing temperature increased during the low-temperature annealing stage. However, as the annealing temperature further increased from 800 to 1100 °C, the FWHM of Peak B decreased rapidly, suggesting the significant thermal decomposition of the Ni_3C at the high annealing temperatures. Peak C in Fig. 4a was ascribed to the Ni(200) peak. It was shown that Peak C shifts obviously as the RTP temperature changes. As the temperature increased from room temperature to 400 °C, the position of the Ni(200) peak gradually shifted to a lower 2θ angles, indicating the increased tensile strain in the Ni lattice due to the diffusion of a-C and the formation of Ni_3C. However, as the temperature further increased up to 800 °C, the Ni(200) peak position shifted back to a higher 2θ angle, suggesting that the lattice stress was released at around 800 °C. It is believed that the stress release resulted from the decomposition of Ni_3C into graphitic carbon and Ni. As the annealing temperature further increased to 1100 °C, the Ni(200) peak shifted to a lower 2θ angle again, indicating the increased lattice strain of the Ni(200) phase. The increased strain was ascribed to the formation of graphene, which wrapped the remaining Ni nanoparticles and induced an internal lattice strain of Ni. It is noted that the XRD signal of Ni_3C phase was also observed in the samples annealed at 800 and 1000 °C, which confirms the existence of Ni_3C phase during the graphene formation process. The existence of Ni_3C phase in the samples annealed at 800 and 1000 °C should be ascribed to incomplete decomposition of Ni_3C phase during the short and rapid heating step.

Based on the temperature-resolved AES depth profiling and the GAXRD characterization, an RTP graphene growth mechanism is suggested. In the initial RTP heating period from room temperature to 400 °C, the a-C sandwich layer gradually diffuses into the Ni lattice and forms metastable hcp Ni_3C at the interface region. As the RTP annealing temperature goes above 400 °C, the Ni_3C at the interface region becomes unstable and starts to decompose into graphitic C and Ni. At the same time, the released carbon atoms continuously diffuse up from the interface region towards the Ni surface region *via* alternative Ni_3C formation and decomposition until they reach the Ni surface. Then, as a result of the bulk-to-surface carbon diffusion, significant Ni evaporation *via* the decomposition of Ni_3C at the surface occurs at high annealing temperatures above 800 °C. According to the Ni–C phase diagram, Ni_3C only exists up to around 1000 °C at atmospheric pressure and starts to decompose at temperatures above 400 °C.[20,21] In order to obtain in-depth understanding of the graphene formation in RTP processes, we have cooperated with theoretical chemists and conducted the atomic-scale mechanism investigation *via ab initio* molecular dynamics (AIMD) simulations in the rapid thermal processing (RTP) (which will be published elsewhere). According to the simulation results the nickel carbide can assist the graphene formation and indeed plays an important role in the RTP processes.[22] Also we have found a relevant work on nickel carbide transformation into graphene by other group,[23] which is in line with our claim that the nickel carbide plays an important role in graphene formation. Therefore, it would be

reasonable to suggest that the metastable Ni_3C would act as an intermediate phase converting amorphous carbon into ordered graphitic lattices and be responsible for the autonomous Ni evaporation at an elevated temperature. During the high-temperature RTP annealing stage (800–1100 °C), the Ni evaporation facilitated by the Ni_3C decomposition continues and leads to a reduced thickness of the Ni top layer. By the end of the RTP annealing process, the Ni top layer has evaporated, leaving graphene layers and residue of Ni nanoparticles on the dielectric substrates. Therefore, the graphene growth in the RTP annealing process follows a solid-state transformation mechanism from a-C to graphene 2D crystal *via* the formation, decomposition and evaporation of Ni_3C.

It was discovered that the RTP heating profiles, including the heating rate and the RTP annealing temperature, significantly influenced the graphene growth in the RTP process. Fig. 5a shows a contour map of graphene quality as a function of the RTP temperature and the heating rate. Interestingly, we found that RTP graphene growth favors a heating rate at about 15 °C s^{-1} (given the sample structure of Ni (65 nm)/a-C (5 nm), and the annealing temperature of 1100 °C) (Fig. S2 and S3†). Both higher and lower heating rates (such as 1 and 25 °C s^{-1}) resulted in less Ni evaporation and lower graphene quality than those at 15 °C s^{-1}. The existence of an optimal RTP heating rate at 15 °C s^{-1} can be understood by studying the thermal dynamics of the RTP process including the Ni_3C decomposition and the carbon diffusion within the Ni film. Based on the Kissinger method,[24,25] the relationship between Ni_3C decomposition temperature and the RTP heating rate can be defined as given in eqn (1) and plotted in Fig. 5c.

$$\ln\left(\frac{R}{T_p^2}\right) = -\left(\frac{\Delta E}{K_B T_p}\right) + A \quad (1)$$

where, T_p is the Ni_3C decomposition peak temperature, R is the heating rate, ΔE is the activation energy for Ni_3C decomposition (204 kJ mol^{-1}),[25] K_B is the Boltzmann constant, and A is a constant (~15.4).[25] As the heating rate increases from 0.01 to 25 °C s^{-1}, the decomposition temperature of Ni_3C increases logarithmically from 460 to 673 °C. In our RTP process, the Ni_3C decomposition threshold temperature is estimated to be ~650 °C with the optimal heating rate of 15 °C s^{-1}.

By applying Fick's second law of diffusion, the carbon diffusion length during the RTP process can be calculated (Fig. 5d and ESI†). During RTP heating from room temperature to 465 °C (the onset temperature for Ni_3C to start decomposition),

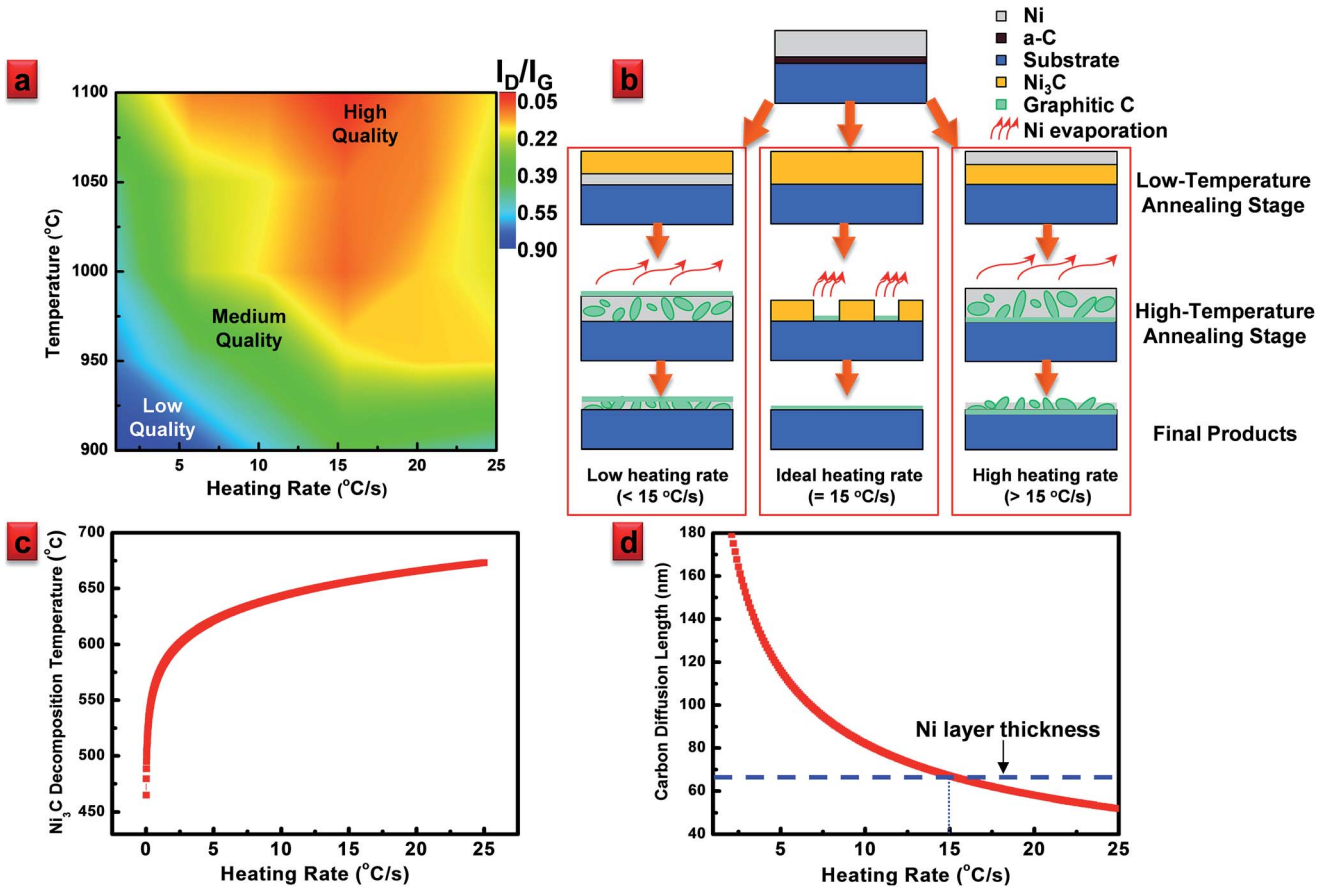

Fig. 5 Analysis of graphene growth dynamics in the RTP growth process. (a) A contour map of graphene quality (represented by I_D/I_G ratio) as functions of RTP temperature and heating rate. (b) Schematic of the solid-state RTP growth processes with low, ideal and high heating rates for graphene synthesis. (c) Plot of Ni_3C decomposition temperature as a function of heating rate. (d) Plot of carbon diffusion length as a function of heating rate.

the carbon diffusion length through the Ni layer decreases as the heating rate increases. The diffusion length reaches about 65 nm (the Ni layer thickness used in the study) when the heating rate is set to 15 °C s^{-1}, which suggests that the whole Ni layer is fully carburized before the Ni_3C decomposition. However, if the heating rate further increases above 15 °C s^{-1}, the carbon diffusion length is less than the Ni layer thickness of 65 nm, which means the surface region of the Ni layer is not fully carburized before the onset of Ni_3C decomposition. Therefore, the carbon-induced Ni evaporation under a high heating rate above 15 °C s^{-1} will be limited due to the lack of Ni_3C formation at the surface region. On the other hand, when the heating rate decreases below 15 °C s^{-1}, the decomposition peak temperature of Ni_3C decreases quickly, as shown in Fig. 5c. Therefore, although the Ni film can be fully carburized under the low heating rate (<15 °C s^{-1}), the as-formed Ni_3C starts to decompose at a relatively low temperature as the thermal energy is not high enough to activate the formation of graphene growth, resulting in the preferable formation of glassy carbon instead of the formation of graphene under the low heating rates. Therefore, to achieve high-quality graphene growth, it is important to control the RTP heating rate (set to 15 °C s^{-1} in our studies with a fixed 65 nm Ni layer) to ensure the Ni_3C decomposition and graphene formation occur simultaneously in the high-temperature RTP annealing stage. Fig. 5b is an illustration of graphene growth with three different heating rates in the RTP processes. Based on the growth model, it is expected that faster growth of graphene at a lower substrate temperature is potentially feasible by using thinner Ni/C films and certain nonconventional heating techniques (*e.g.*, flash annealing or laser annealing).[26,27]

Conclusions

In conclusion, a single-step transfer-free RTP method was investigated for wafer-scale growth of high-quality graphene. It was discovered that the formation, decomposition and evaporation of metastable hcp Ni_3C is critical to the successful solid-state transformation from a-C to graphene 2D crystal in RTP process with high heating rates (*e.g.* 15 °C s^{-1}). The discovery of this solid-state graphene growth mechanism can be used as a guide for the rapid graphene growth based on transition metals such as Ni, and it will open new opportunities for high-quality and low-cost graphene synthesis, paving the way toward many practical applications.

Acknowledgements

This research work was financially supported by the National Science Foundation (CMMI 1265122, CMMI 1129613, and CMMI 1068510) and Nebraska Center for Energy Sciences Research. The authors are grateful to J. Brehm for the high-quality graphic design. The graphene growth process developed in this study has a patent pending. A portion of this research was conducted at the Center for Nanophase Materials Sciences, which is sponsored at the Oak Ridge National Laboratory by the Scientific User Facilities Division, Office of Basic Energy Sciences, and the U.S. Department of Energy.

Notes and references

1 A. K. Geim and K. S. Novoselov, *Nat. Mater.*, 2007, **6**, 183–191.
2 A. K. Geim, *Science*, 2009, **324**, 1530–1534.
3 K. S. Novoselov, V. I. Fal'ko, L. Colombo, P. R. Gellert, M. G. Schwab and K. Kim, *Nature*, 2012, **490**, 192–200.
4 K. S. Novoselov, A. K. Geim, S. V. Morozov, D. Jiang, Y. Zhang, S. V. Dubonos, I. V. Grigorieva and A. A. Firsov, *Science*, 2004, **306**, 666–669.
5 R. Munoz and C. Gomez-Aleixandre, *Chem. Vap. Deposition*, 2013, **19**, 297–322.
6 Z. Z. Sun, Z. Yan, J. Yao, E. Beitler, Y. Zhu and J. M. Tour, *Nature*, 2010, **468**, 549–552.
7 J. A. Rodriguez-Manzo, C. Pham-Huu and F. Banhart, *ACS Nano*, 2011, **5**, 1529–1534.
8 R. S. Weatherup, C. Baehtz, B. Dlubak, B. C. Bayer, P. R. Kidambi, R. Blume, R. Schloegl and S. Hofmann, *Nano Lett.*, 2013, **13**, 4624–4631.
9 K. L. Saenger, J. C. Tsang, A. A. Bol, J. O. Chu, A. Grill and C. Lavoie, *Appl. Phys. Lett.*, 2010, **96**, 153105.
10 M. Hupalo, E. H. Conrad and M. C. Tringides, *Phys. Rev. B: Condens. Matter Mater. Phys.*, 2009, **80**, 041401(R).
11 W. Xiong, Y. S. Zhou, L. J. Jiang, A. Sarkar, M. Mahjouri-Samani, Z. Q. Xie, Y. Gao, N. J. Ianno, L. Jiang and Y. F. Lu, *Adv. Mater.*, 2013, **25**, 630–634.
12 W. Kern, *Handbook of semiconductor wafer cleaning technology: science, technology and applications*, Noyes Publications, Park Ridge, N.J., U.S.A., 1993.
13 D. L. Leslie-Pelecky, X. Q. Zhang, S. H. Kim, M. Bonder and R. D. Rieke, *Chem. Mater.*, 1998, **10**, 164–171.
14 S. Sinharoy, M. A. Smith and L. L. Levenson, *Surf. Sci.*, 1978, **72**, 710–718.
15 K. Yan, H. L. Peng, Y. Zhou, H. Li and Z. F. Liu, *Nano Lett.*, 2011, **11**, 1106–1110.
16 X. S. Li, W. W. Cai, J. H. An, S. Kim, J. Nah, D. X. Yang, R. Piner, A. Velamakanni, I. Jung, E. Tutuc, S. K. Banerjee, L. Colombo and R. S. Ruoff, *Science*, 2009, **324**, 1312–1314.
17 A. Dahal and M. Batzill, *Nanoscale*, 2014, **6**, 2548–2562.
18 M. S. Xu, D. Fujita, J. H. Gao and N. Hanagata, *ACS Nano*, 2010, **4**, 2937–2945.
19 J. Shi and O. Nittono, *J. Mater. Sci. Lett.*, 1996, **15**, 928–930.
20 M. Singleton and P. Nash, *J. Phase Equilib.*, 1989, **10**, 121–126.
21 J. J. Lander, H. E. Kern and A. L. Beach, *J. Appl. Phys.*, 1952, **23**, 1305–1309.
22 S. Chen, W. Xiong, Y. S. Zhou, Y. F. Lu and X. C. Zeng, *ACS Nano*, 2015.
23 J. Lahiri, T. Miller, L. Adamska, I. I. Oleynik and M. Batzill, *Nano Lett.*, 2011, **11**, 518–522.
24 H. E. Kissinger, *Anal. Chem.*, 1957, **29**, 1702–1706.
25 Y. H. Leng, L. Xie, F. H. Liao, J. Zheng and X. G. Li, *Thermochim. Acta*, 2008, **473**, 14–18.
26 W. C. Yen, H. C. Lin, J. S. Huang, Y. J. Huang and Y. L. Chueh, *Sci. Adv. Mater.*, 2014, **6**, 1–8.
27 W. Xiong, Y. S. Zhou, W. J. Hou, L. J. Jiang, Y. Gao, L. S. Fan, L. Jiang, J. F. Silvain and Y. F. Lu, *Sci. Rep.*, 2014, **4**, 4892.